ACS APPLIED MATERIALS & INTERFACES

Research Article

Cite This: ACS Appl. Mater. Interfaces XXXX, XXX, XXX−XXX

www.acsami.org

Scaling Atomic Layer Deposition to Astronomical Optic Sizes: Low-Temperature Aluminum Oxide in a Meter-Sized Chamber

David M. Fryauf,*[,†] Andrew C. Phillips,[‡] Michael J. Bolte,[§] Aaron Feldman,[∥] Gary S. Tompa,[∥] and Nobuhiko P. Kobayashi[†]

[†]Nanostructured Energy Conversion Technology and Research (NECTAR), [‡]University of California Observatories, and [§]Department of Astronomy and Astrophysics, University of California Santa Cruz, Santa Cruz, California 95064, United States

[∥]Structured Material Industries Inc, Piscataway, New Jersey 08854, United States

ABSTRACT: Atomic Layer Deposition (ALD) is very attractive for producing optical quality thin films, including transparent barrier films on metal-coated astronomical mirrors. To date, ALD of mirror coatings has been limited to relatively small-sized substrates. A new ALD tool has been designed, constructed, and tested to apply uniform protective coatings over a 0.9 m diameter substrate in a 1 m diameter scale deposition plane. The new tool, which we have named the meter scale ALD system (MSAS), employs a unique chamber design that isolates a large substrate surface to be coated by utilizing the substrate as a wall of the reaction chamber. The MSAS is mechanically designed to be rapidly reconfigurable for selective area coating of custom substrates with arbitrary shape, size, and permanent backside hardware attachments. The design, implementation, results, and future applications of this new tool are discussed for coating large-area optical substrates, specifically protective coatings for silver mirrors, and other future large astronomical optics. To demonstrate the potential of this new design, aluminum oxide was deposited by thermal ALD using trimethylaluminum and water at a low reaction temperature of 60 °C. Growth rate and uniformity, which are dependent on precursor pulse times and chamber purge times, show that the two half-reactions occur in a saturated regime, matching typical characteristics of ideal ALD behavior. Aluminum oxide deposition process parameters of the MSAS are compared with those of a conventional 100 mm wafer-scale ALD tool, and saturated ALD growth over the 0.9 m substrate is realized with a simple scaling factor applied to precursor pulse and purge times. This initial test shows that lateral thickness uniformity across a 0.9 m substrate is within 2.5% of the average film thickness, and simple steps to realize 1% uniformity have been identified for next growths. Results show promising application of transparent robust dielectric films as uniform coatings across large optical components scaled to meter-sized substrates.

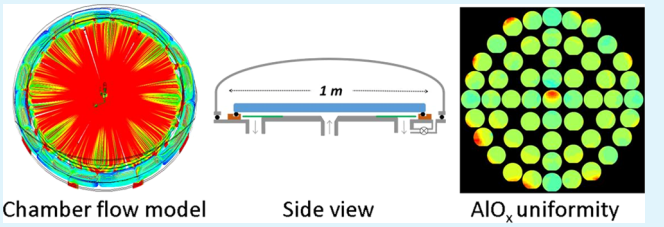

KEYWORDS: *ALD, aluminum oxide, corrosion barrier, protected silver mirrors, reflective coatings, mirror, ALD chamber, ALD reactor, scalable ALD*

1. INTRODUCTION

Durable broad-band mirror coatings of protected silver (Ag) are highly sought for ground-based astronomical telescopes. While aluminum mirrors are widely used, Ag offers significant performance advantages because of its superior reflectivity at visible-light wavelengths and lower emissivity at thermal infrared wavelengths. Currently, the Gemini telescopes are the only Ag-based mirrors with reported long-lived protecting coatings,[1−4] and the fact that so few ground-based telescopes use Ag-based mirrors demonstrates the elusiveness of viable Ag-based mirrors. Even the Gemini coating comes with the cost of sacrificing deep blue and UV portions of the spectrum because of unwanted absorption primarily from the nickel−chromium nitride adhesion layer,[1,2] which is an unacceptable compromise for many astronomical programs. The Advanced Coatings Lab of the University of California Observatories (UCO) has been identifying and developing high-performance coatings useful for astronomical optics.[5−9] The Thirty-Meter Telescope (TMT) project has stringent requirements of broadband high reflectivity ($0.34 < \lambda < 28\ \mu m$[10]) and "lifetimes" of 5−10 years between recoating, which has supplied the motivation for this research and development of durable Ag mirror coatings.

Large telescope optical components have traditionally been coated using physical vapor deposition (PVD). Robust uniform films of precise thickness can be applied using PVD for many optical applications including reflective,[11−15] anti-reflective (AR),[16−18] and transparent barrier coatings.[19−21] However, because of extrinsic factors such as the necessary large deposition area, non-cleanroom environment during substrate cleaning, and subsequent film deposition, pinholes are unavoidable and can be a significant problem as they provide moisture and other chemicals a means to permeate into the metal thin film, leading to corrosion.[22−26] Because

Received: June 22, 2018
Accepted: November 12, 2018
Published: November 12, 2018

DOI: 10.1021/acsami.8b10457
ACS Appl. Mater. Interfaces XXXX, XXX, XXX−XXX

PVD conditions require line-of-sight deposition, high aspect ratio substrate defects, including pinholes, may not be completely encapsulated. Atomic layer deposition (ALD) offers an ideal solution of pinhole-free barrier overlayers because of its excellent conformality over complex three-dimensional structures.[27−31] Although it has been shown that Ag mirrors protected by both PVD-and ALD-based barrier films are prone to hygroscopic air borne particles inducing corrosion,[32] the low-stress, amorphous nature of ALD films is expected to improve overall mechanical integrity by reducing or eliminating crystalline grain boundaries and defects in barrier overlayers, which serve as diffusion pathways for corrosion of the underlying Ag.[32−35] In addition, ALD produces smooth films with precise thickness and excellent uniformity, which is critical to achieve uniform spectral response across large-area optical substrates. High-quality dielectric films are realized by ALD, with processing temperatures lower than conventional chemical vapor deposition (CVD) and vacuum requirements less stringent than high-vacuum conditions necessary for PVD. These beneficial film properties and processing conditions make ALD an attractive technique for depositing robust transparent dielectric thin films on large-area optics. Potential applications of ALD coatings to large-area substrates, besides protective barriers on first surface mirrors, include AR coatings on lenses also used in astronomy, window filters, and protective AR coatings.

ALD is a specific subset technique of CVD that relies on repetitive cycles of chemical half-reactions to deposit monolayers of a thin film. In an ideal reaction, each cycle uniformly and conformally deposits a monolayer on every surface in the vacuum chamber, and the total film thickness is linearly dependent on the number of cycles. The well-understood, nearly ideal reaction of trimethylaluminum (TMA) and water (H_2O) to form aluminum oxide (AlO_x),[28−31] which is also the reaction demonstrated in this work, can be described in four steps: (1) introduction of TMA vapor into the chamber, which chemisorbs to surfaces by the methyl ligand reaction with surface hydroxyl bonds, releasing methane (CH_4) as a byproduct, (2) chamber-purge to remove CH_4 and excess TMA with the exception of a chemically bonded monolayer of dimethylaluminum hydroxide on all exposed surfaces, (3) introduction of H_2O vapor into the chamber to react with the methyl-terminated monolayer, removing remaining methyl ligands, forming a monolayer of AlO_x on all surfaces with additional CH_4 byproduct, and (4) chamber-purge to remove byproducts and excess H_2O vapor, leaving a uniform hydroxyl-terminated AlO_x surface ready for the next cycle. The ALD process ideally operates in "saturated growth mode;" each precursor dose step is excessive enough to create a saturating monolayer on every surface in the chamber, and each purge step is long enough to remove all excess precursor from the previous dose step. Once all process parameters have been adequately tuned to achieve saturated growth mode, small variations in pulse or purge conditions will not affect the resulting growth rate of the ALD reaction.

Many other metals and compound materials across the periodic table have been deposited by ALD with a wide range of properties.[36] Specialized techniques, such as plasma-enhanced ALD, enable an even wider range of material compositions and thin-film properties.[37] The capability of ALD to deposit films on a variety of substrates, including complex high-aspect ratio microstructures and surfaces with different chemical reactivity, has been theoretically analyzed and modeled.[38,39] The ultrahigh aspect ratio conformal films deposited by ALD are commonly utilized for various applications including semiconductor processing procedures.[40−43] ALD has become widely popular in materials science applications such as device packaging, semiconductor passivation, transistor gate dielectrics, chemical catalytic surface treatment, optical coatings, energy storage devices, and protective barriers.[28,36,44,45] Several variations of the ALD technique have become standardized industry tools in semiconductor processing for single wafers and wafer batches.[46] Large-area ALD processes have been developed for nonwafer substrates, often utilizing a high-throughput technique known as spatial ALD,[47] with the largest published substrate size of 1.2 m.[48,49] Spatial ALD, in contrast to the temporal ALD process previously described, utilizes the same four step chemistry process by simultaneously running all four steps (TMA pulse, TMA purge, H_2O pulse, and H_2O purge) in separated localized zones of a reaction chamber while the substrate to be coated repeatedly moves across the four reaction zones to obtain a desired film thickness. Spatial ALD techniques are gaining popularity with large-area substrates in semiconductor and display manufacturing due to deposition rates several orders of magnitude faster than temporal ALD and scalability compatible with manufacturing line processes, led by companies such as Beneq[50] and SoLayTec.[51] While spatial ALD is a technically effective and industrially competitive solution for coating large flat substrates, they are not currently capable of coating large-area substrates with any curvature, such as concave or convex optical surfaces. Furthermore, existing spatial ALD processing equipment cannot handle substrates with bulky features permanently attached to the backside, such as the mounting hardware used in astronomical telescope mirrors. Because existing spatial ALD tools cannot be easily reconfigured to coat nonflat substrates or substrates with bulky sensitive backside attachments, there have been no demonstrations of ALD-based coating technology which could be practically applied to astronomical telescope optics.

In this paper, we demonstrate deposition of AlO_x at a desirable low temperature of 60 °C on silicon wafers using a ∼1 m wide economical commercial glass tabletop as a sample-holding substrate. Aluminum oxide was chosen as a demonstration thin-film barrier material for this initial experiment because of the previous success observed with AlO_x deposited by ALD, its acceptable transmission properties, its chemical and mechanical durability, and its standardized acceptance of an ideal and well-documented ALD chemistry process.[27−29] This work introduces a new implementation of low-temperature thermal ALD capable of coating meter-sized substrates with the ability to be rapidly reconfigured to coat custom optics with arbitrary shape, size, and backside hardware attachments. The key concept of this new chamber design was originally introduced by Phillips et al.,[9] describing an ALD chamber where the reaction volume was kept small by using the substrate as part of the reaction chamber, and initial results of the chamber deposition testing have been presented.[52] Film deposition which utilizes a substrate to be coated as a chamber wall has been previously demonstrated using atmospheric pressure ALD onto a ∼7.5 cm diameter area of a car windshield, but the coated surface perimeter was isolated by a purge gas curtain instead of an O-ring.[53] Conventional coupon-sized substrates (∼2 cm^2) have also been coated in a traveling wave ALD chamber under vacuum in a similar

DOI: 10.1021/acsami.8b10457
ACS Appl. Mater. Interfaces XXXX, XXX, XXX−XXX

configuration using the substrate as a wall of the chamber.[54] However, we believe that the substrate/chamber wall design employed for the meter scale ALD system (MSAS) is the first demonstration of a CVD-based coating technique that can be practically applied to existing large curved substrates with large backside fixtures in place, such as segments of a telescope primary mirror like those required for the TMT project.

2. EXPERIMENTAL DETAILS

2.1. Reactor Design. The MSAS chamber, illustrated in Figure 1a, is a hybrid design that utilizes the advantages of both vertical and horizontal flow chamber designs to optimize uniform symmetrical gas flow and minimize duty cycle time by maintaining minimal chamber volume. Process gas flows vertically into the center of the chamber perpendicular to the substrate to be coated, disperses outward along a tapered conical entry port, then flows horizontally, confined to the high-aspect ratio chamber, around the outer edge of the flow diversion sheet next to the chamber edge O-ring, and is finally exhausted through eight radially symmetrical KF-40 ports. Such a hybrid design creates a relatively small chamber volume with a high aspect ratio of lateral flow, like a horizontal flow traveling wave reactor, but also with the radial symmetry, concentric gas flow, and increased gas-to-substrate collisions of a vertical reactor.[39,53,55]

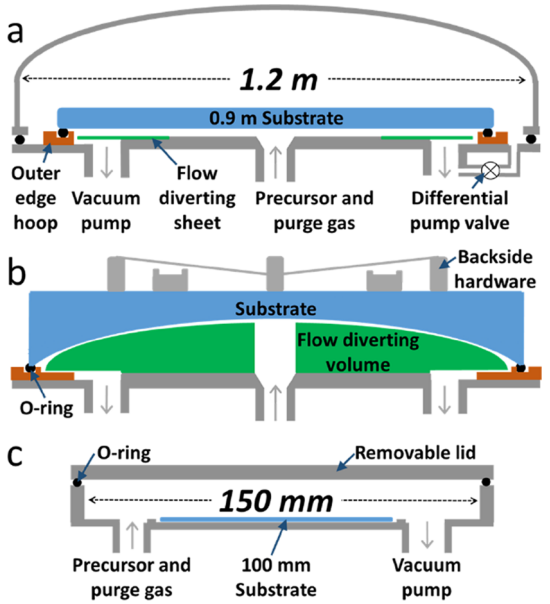

Figure 1. (a) Illustration of the MSAS chamber cross section viewed from the side. Gas flows upward into the chamber center, diverts with radial symmetry at the 0.9 m substrate chamber wall (blue), passes over the flow diverting sheet (green) to ensure uniform deposition to the O-ring at the outer edge hoop (orange), and finally exits through eight symmetrically arranged exhaust ports. A differential pumping valve regulates pressure on the substrate backside. (b) Potential configuration of the MSAS chamber with no top dome lid, custom flow diverting volume hardware, and outer edge hoop to hold a larger concave optic with backside hardware isolated from the reaction chamber. (c) Illustrated at larger magnification for comparison, a conventional horizontal ALD chamber with lateral gas flow across a 100 mm substrate.

The substrate/chamber wall design of the MSAS has two significant advantages for realizing ALD thin-film coatings on large substrates. First, the ability to maintain relatively small reaction process chamber volume for various custom optical surfaces allows for shorter process gas purge times and therefore faster deposition rates. Second, large substrate front surfaces are coated while isolating the arbitrarily large volumes and sensitive backside features from reaction chemistry, heating, and vacuum. These two advantages, illustrated in Figure 1a,b, are critical for demonstrating practical routine coating application in an observatory environment. The chamber baseplate design allows rapid reconfiguration with interchangeable parts: modular detachable components that can be custom-designed to accommodate substrate surfaces with arbitrary shapes and sizes to establish a small reaction volume regardless of geometrical features of a substrate. Specifically, the currently installed hoop containing the edge O-ring which seals to the baseplate with a 0.9 m O-ring is replaceable, and the flow-diverting sheet, which is bolted into the baseplate to guide gas flow from the chamber center to the edge O-ring seal, can be replaced by a larger flow diverting volume-filling piece to maintain a small reaction chamber size and therefore lower cycle times.

Figure 1a illustrates the MSAS chamber with replaceable custom hardware components in its current configuration to coat a flat circular 0.9 m glass substrate, as applied to this work. However, this chamber configuration can be modified to accommodate more complex large optical substrates (example illustrated in Figure 1b), such as an oval-shaped concave substrate (telescope tertiary fold mirror), a convex lens, or a donut-shaped substrate with a central hole such as a single-piece primary mirror. Substrates with through-holes can still act as a chamber wall with the use of an additional custom hardware piece and O-ring to cap and seal the hole from either the front or back side of the substrate. Backside capping of substrate holes would rely on less hardware and allow the inside of the hole to be coated, but it would increase the chamber volume and the applied force on the substrate backside due to differential pressure when applying vacuum; this technique would be best applied to small through-holes in thick substrates. Capping substrate holes from the font side would require hardware designed to support the weight and pressure-induced deflection of the substrate under vacuum while still maintaining uniform symmetrical gas flow in the chamber, but it would minimize the reaction chamber volume; this technique would be best applied to large holes in thin substrates. Large-area astronomical optics such as the examples previously described are typically designed with a ~3 mm beveled outer edge to function as a safe contact point during transportation, coating, and assembly processes. This beveled edge makes such substrates easily compatible with the MSAS reconfigurable hardware mounting mechanism by providing a precise edge profile to seal with using a custom O-ring and outer hoop, thereby eliminating any edge exclusion in the coating process. The hardware configuration used in this study to demonstrate MSAS coating uniformity on an arbitrary large-area substrate excludes 1.5 cm of the substrate edge with the O-ring. However, practical coatings applied to large-area astronomical optics are expected to have negligible edge exclusion with proper design of the reconfigurable hardware.

The top dome chamber lid of the MSAS, illustrated in Figure 1a, can be used to control backside pressure and temperature of sensitive substrates, but the top dome is not necessary for deposition on the downward-facing active surface of a substrate. When backside temperature and pressure control are not necessary or desired, the MSAS system can operate without the top dome and still isolate and coat large surfaces of arbitrarily thick substrates/objects with large volumes and backside features. This substrate/chamber relationship contrasts with a conventional ALD chamber design, illustrated in Figure 1c, which can only support a finite substrate volume in an enclosed chamber. In Figure 1c, it is apparent that a substrate cannot be thicker than the height of the chamber, and the substrate volume obviously cannot exceed the volume of the chamber. In contrast considering the MSAS, if a vacuum-tight seal can be formed between the substrate surface to be coated and an O-ring supported by a custom edge hoop, then the size, shape, and backside features of the substrate are only limited by the supporting facilities housing the MSAS.

Computational fluid dynamic (CFD) calculations were simulated using various chamber geometries in the design of the MSAS to optimize film uniformity with the larger scale of ALD process gas flow dimensions. Figure 2 shows gas velocity modeled in the MSAS chamber, using10 sccm argon (Ar) flow into the existing

DOI: 10.1021/acsami.8b10457
ACS Appl. Mater. Interfaces XXXX, XXX, XXX−XXX

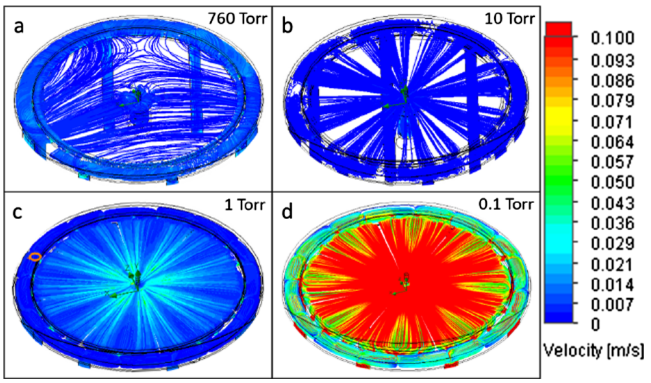

Figure 2. CFD simulations showing 2D uniformity of MSAS chamber gas flow velocity at four different pressures: (a) 760, (b) 10, (c) 1, and (d) 0.1 Torr. Moderate non-uniformity with eight-fold symmetry develops near the chamber edge in relation to the eight exhaust ports.

interchangeable hardware demonstrated in this study with a fixed conductance gap (chamber height) of 5 mm, with output pressure at four different orders of magnitude: 760, 10, 1, and 0.1 Torr. At lower operating pressures, gas velocity increases, and a moderate eight-fold symmetry is observable which correlates with the eight exhaust ports under the flow diversion sheet with higher gas velocity directly above the exhaust ports. It is apparent that the geometrical dependence of gas velocity with exhaust port position varies at different orders of magnitude in operating pressure, where this dependence is strongest at the low operating pressure of 0.1 Torr in Figure 2d. CFD results shown in Figure 2d at this lower pressure in the mTorr range are most relevant for this study because this best resembles the operating pressure of most ALD systems, including the MSAS demonstrated in this work (operating pressure of 125 mTorr). Additional CFD modeling (not shown) has demonstrated that modified flow diverting sheet geometries may be used to further mitigate gas flow patterns and non-uniformity across the chamber and is expected to be implemented in future work using the MSAS chamber.

The symmetrical eight-fold gas velocity pattern seen in Figure 2 is geometrically correlated with the pattern of the eight exhaust ports, each with diameter of 3.5 cm, seen in Figure 3a from the top-down perspective of the chamber baseplate SolidWorks rendering. The eight ports are coupled by four T-connections into four KF-40 lines, and these four lines are coupled into one KF-40 exhaust port below the baseplate, as seen from the upward-facing 3D perspective of Figure 3b in the SolidWorks rendered CAD model of the exhaust system. The eight exhaust paths from each port are matched in length and are evenly distributed around the baseplate to ensure symmetrical conductance during process pumping. The configuration of the exhaust ports in the baseplate allows for insertion of additional flow diverting hardware to further homogenize the exhaust flow, which will be explored in future work.

Figure 3c shows the MSAS deposition tool installed at the University of California Santa Cruz (UCSC) with a 0.9 m diameter tempered glass tabletop mounted as a substrate (Figure 3d). The outer chamber top dome lid (140 kg) is hoisted by an electric chain-drive motor suspended by an A-frame gantry spanning across the square gas delivery frame. The square gas delivery frame also contains the exhaust and vacuum pump systems, and it supports the weight of the assembled ~460 kg chamber baseplate, optic to be coated, and the outer chamber top dome lid. The electronics control rack with customized computer interface sits adjacent to the gas delivery frame. All MSAS system components were designed and assembled at SMI Inc. where many other custom state-of-the-art materials deposition and processing tools have been developed for various applications [www.SMICVD.com].

2.2. Saturated ALD Growth Mode Calibration. All AlO_x depositions in the MSAS utilized TMA of 98% purity purchased from Strem Chemicals as the aluminum precursor and deionized water (H_2O) in a refillable stainless-steel ampule as the oxidizer. Both

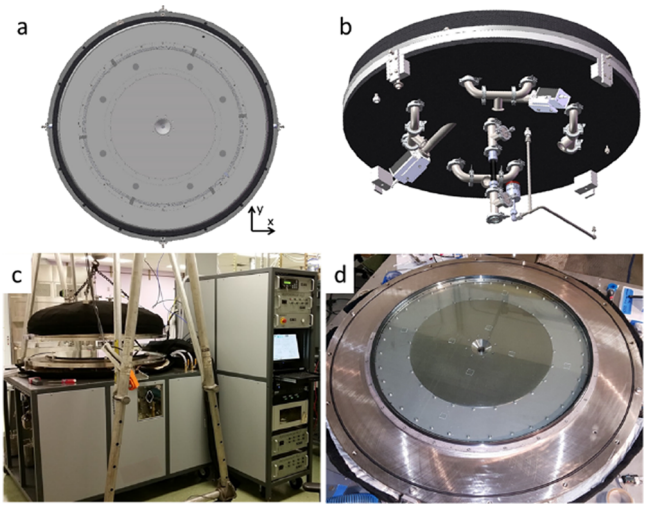

Figure 3. Renderings of the MSAS SolidWorks CAD models show the central gas inlet and eight edge exhaust ports from (a) top-down 2D view and (b) upward-facing 3D perspective. Photographs of the MSAS tool show (c) gas delivery cabinet frame supporting the chamber baseplate, adjacent to an electronics control rack, with the 140 kg heated dome lid which is supported by an A-frame gantry during substrate unloading/loading. (d) Heated baseplate supports the face-down substrate (shown with 0.9 m diameter tempered glass table mounted as a substrate ready to-be-coated or to have wafers attached to the downward face).

precursors were kept at room temperature (21 °C), and precursor vapor pulses were delivered to the chamber by high-speed Swagelok ALD diaphragm valves via separate gas lines with a combined carrier gas flow of 20 sccm Ar. Resistive heater wraps maintain the temperature of gas delivery lines at 150 °C upstream of the deposition chamber. The baseplate temperature, controlled by eight 1 kW resistive heater bars mounted symmetrically around the underside of the baseplate, was held at 63 °C. The top dome lid temperature, controlled by a resistive heater blanket custom-shaped to the outer geometry of the dome, is also set to 63 °C to establish a consistent temperature of 60 °C as measured on the backside of the glass substrate by a K-type thermocouple during deposition. Upon reaching a measured substrate backside temperature of 60 °C, all depositions were preceded with a 30 min stabilization step to ensure thermal equilibrium while both TMA and H_2O precursor lines were purged with 20 sccm Ar gas. At these conditions, operating pressure of the active deposition chamber was 125 mTorr for each experiment, while the backside chamber pressure was held at 50 Torr to apply an estimated ~450 kg of total force (0.967 psi) to the backside of the glass substrate. This pressure, 6.6% of atmospheric pressure, was chosen to reduce stress to the glass substrate while still maintaining adequate compression between the glass edge and O-ring to ensure a good vacuum seal. However, this reduced backside pressure still causes the glass substrate to deflect downward and contact the center of the chamber baseplate. Therefore, to precisely control total deflection of the glass substrate from the regulated backside pressure without damaging the glass or the silicon samples mounted to the glass surface, four mechanical standoff washers were taped to the glass in a square pattern 7 cm from the substrate center. The mechanical support provided by these round standoffs (2 mm high and 1 cm diameter) around the gas inlet were positioned to minimize any disturbing effect of changing gas flow uniformity on adjacent silicon substrates. By using these standoffs to fix the chamber height (conductance gap) to 2 mm at the center, we assume that the variation in chamber height across the substrate due to deflection increases from 2 mm at the chamber center up to 5 mm at the chamber edge. Deflection-limiting standoffs may not be necessary in future work if pressure-induced stress on the substrate backside is further reduced with the use of mechanical clamps around the

DOI: 10.1021/acsami.8b10457
ACS Appl. Mater. Interfaces XXXX, XXX, XXX−XXX

substrate edge as a substitute for a high backside pressure, which would still provide adequate compression of the O-ring seal. While the use of standoffs to control substrate deflection and chamber height were necessary for this experiment using a relatively thin piece of large glass as a test substrate, we expect that substrate deflection will be negligible for practical MSAS coatings applied to astronomical optic substrates, because the custom glass substrates utilized in astronomy are at least 5 cm thick.

The tempered glass substrate used to form the deposition chamber had a diameter of 0.93 m and thickness of 1.3 cm. Although the actual substrate diameter is measured at 0.93 m, the 0.9 m diameter O-ring along the edge creates a seal with the glass substrate which excludes 1.5 cm of the outer edge, and therefore all film depositions are discussed with an effective substrate size of 0.9 m. Silicon wafers of 0.5 mm thickness were attached to the glass substrate surface using Kapton tape so that deposited films could be measured with spectroscopic ellipsometry. This study refers to the glass surface as the substrate; however, all measurements were taken from AlO_x films deposited on silicon wafers or coupons taped to the substrate. Spectroscopic ellipsometry and reflectometry measurements at incident angles of 4 and 70° over a 330−938 nm wavelength range were taken using a FilmTek 2000 PAR-SE (Scientific Computing International, Carlsbad, CA) to calculate thickness and refractive indices of AlO_x.

For all deposition experiments testing saturated ALD growth mode, six silicon coupons were mounted on the glass substrate in a straight line from substrate center to the edge next to the O-ring at radial positions of 0, 5, 13, 25, 35, and 45 cm to measure deposition uniformity from the chamber center to the edge, illustrated in Figure 4a. Growth rate and thickness uniformity along the substrate radius were examined while altering pulse and purge times of the TMA and H_2O precursors to calibrate saturated ALD growth mode for the MSAS. All depositions used 300 cycles of the following six steps: TMA pulse, soak, purge, H_2O pulse, soak, and purge. The time-resolved pattern of these steps is illustrated in Figure 4b. Precursor pulse times for TMA and H_2O were held at 300 and 400 ms, respectively, and both precursor purge times were held at 100 s while one pulse or purge time was incrementally decreased to find a change in growth rate or uniformity. Precursor pulse time is commonly used to dictate total precursor exposure (molecular flux, partial pressure) in ALD reactions, and therefore this work utilizes precursor valve opening time as the most direct and precise method of controlling precursor reactant quantity in the reactor. Soak time for both precursors was held at 5 s for all depositions, which was determined to increase uniformity in previous nonsaturated growth experiments. A soak step is defined when a valve is closed downstream of the exhaust assembly to isolate the pump and carrier gas flow is paused to ensure that the precursor pulse has ample time to diffuse evenly throughout the chamber. This constant 5 s soak step is significant in this study for two reasons: (1) it ensures that the entire chamber is exposed to the full precursor dose, which increases precursor efficiency and reliability of quantification of the total amount of precursor exposure, and (2) it disrupts steady-state gas flow patterns, which increases the likelihood of uniform diffusion throughout the large-area chamber and decreases the dependency of film growth uniformity on gas flow patterns.

2.3. Thickness Uniformity Mapping. Using the optimized parameters from Table 1, 600 cycles (~16 h total reaction time) of AlO_x were deposited on 53 100 mm silicon wafers of 0.5 mm thickness to measure high-resolution film uniformity. Using the 0.9 m glass substrate as a wafer holder mounted in the chamber as illustrated in Figure 1a, silicon wafers were arranged symmetrically across the substrate in a radial pattern extending outward from the center which was designed to maximize continuous measurable profiles along a bisecting linear axis and around the circumference of the substrate. Thickness and refractive index of deposited films on each silicon wafer were measured for 60 data points arranged symmetrically from the center to the edge of each 100 mm wafer for a total of 3180 measured points across the entire substrate. The resulting color maps of AlO_x thickness and refractive index at λ = 632 nm offer a more detailed perspective of deposition uniformity in the MSAS when compared to

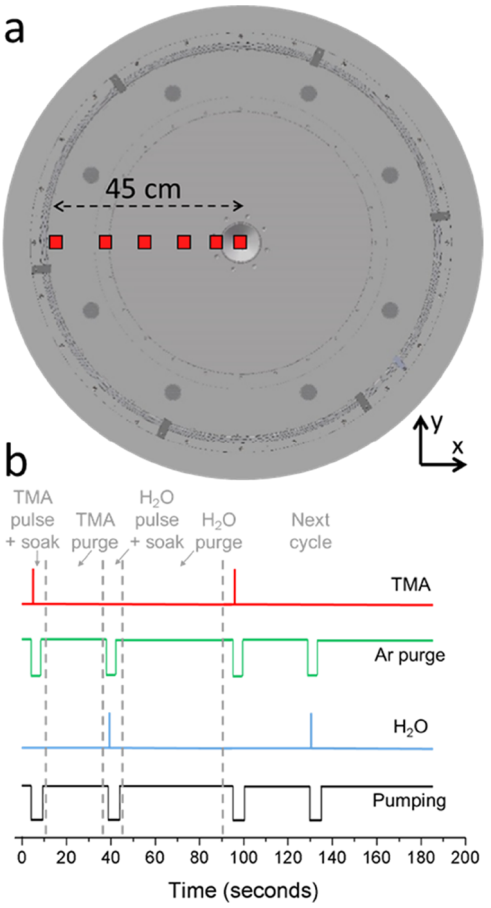

Figure 4. (a) For all depositions calibrating saturated ALD growth mode, silicon sample placement is shown along the substrate 45 cm radius (*x*-axis), illustrated with six red squares overlaid on the top-down 2D CAD rendered image of the MSAS chamber baseplate. (b) Diagram illustrating an example of precursor pulse, soak, and purge times for two cycles of AlO_x deposition. For all combinations of pulse and purge times, TMA or H_2O pulse "soaked" in the chamber for 5 s with the vacuum valve closed and no Ar purge flow. High levels of each line over time indicate "on/open", whereas low levels indicate "off/closed." Dashed vertical gray lines indicate the transitions between steps in a cycle.

characterization of six measured points across the substrate radius illustrated in Figure 4a.

2.4. Comparing Deposition Parameters of 100 mm to 0.9 m Substrate. A small ALD system, using a chamber style illustrated in Figure 1c, has been previously calibrated for AlO_x deposition at 60 °C using TMA and H_2O.[12] After the MSAS deposition parameters were similarly calibrated for saturated ALD growth mode, the two reactors were used to compare process parameters and resulting growth rate and uniformity for 300 cycles of AlO_x. All the deposition parameters used in these two systems, except for the chamber designs and vacuum pumping systems, were set identically to most accurately evaluate the process parameter changes required to scale the 60 °C AlO_x reaction from a 100 mm substrate to a 0.9 m substrate. Given that the chemical reaction in the two reactors is highly comparable, a comparison of the optimized process parameters should have design implications for even larger systems.

Using a small home-built reactor, AlO_x films were deposited on a 100 mm silicon wafer using TMA and H_2O precursors carried by 20 sccm nitrogen purge gas using optimized precursor pulse/purge parameters described in previous work.[27] The conventional small reactor was pumped using an Edwards DP-80 dry pump with a rated pumping speed of 82 (m^3)/h at 75 mTorr and a rated base pressure of 8 mTorr, which performs comparably to the pump used to evacuate

DOI: 10.1021/acsami.8b10457
ACS Appl. Mater. Interfaces XXXX, XXX, XXX−XXX

Table 1. Initial Test Process Parameters and Subsequent Optimized Process Parameters for MSAS Saturated Growth Mode, Including Total Cycle Time

parameter	$t_{TMA\text{-}pulse}$ (ms)	$t_{H_2O\text{-}pulse}$ (ms)	$t_{TMA\text{-}purge}$ (s)	$t_{H_2O\text{-}purge}$ (s)	$t_{TMA\text{-}soak}$ (s)	$t_{H_2O\text{-}soak}$ (s)	cycle time (s)
initial	400	400	100	100	5	5	211
optimized	300	400	30	50	5	5	91

the MSAS, a Leyvac LV80 dry pump with a rated pumping speed of 85 $(m^3)/h$ at 75 mTorr and a rated base pressure of 7.5 mTorr. All other parameters and hardware used in the two reactors were identical (MFCs, ALD valves, precursor, and line temperatures). The resulting film was characterized by ellipsometry spatial mapping to determine growth rate and film uniformity.

3. RESULTS AND DISCUSSION

3.1. Saturated ALD Growth Mode Calibration. Thickness of AlO_x deposited on Si coupons as measured by spectroscopic ellipsometry is shown in Figure 5. 3D color maps (Figures 5a–d) of AlO_x thickness show how thickness and radial uniformity depend on varying precursor pulse/purge times. Figure 5e,f shows AlO_x thickness uniformity as a function of precursor pulse times, where the uniformity percentage value is defined as the maximum variation from the average AlO_x thickness (low uniformity % is desirable). As expected, longer pulse times and purge times yield more uniform deposition. In practice, we want the shortest process times that achieve saturated growth rate, and we found that both average growth rate and thickness uniformity across the chamber must be measured and optimized to ensure that the MSAS is operating in saturated growth mode.

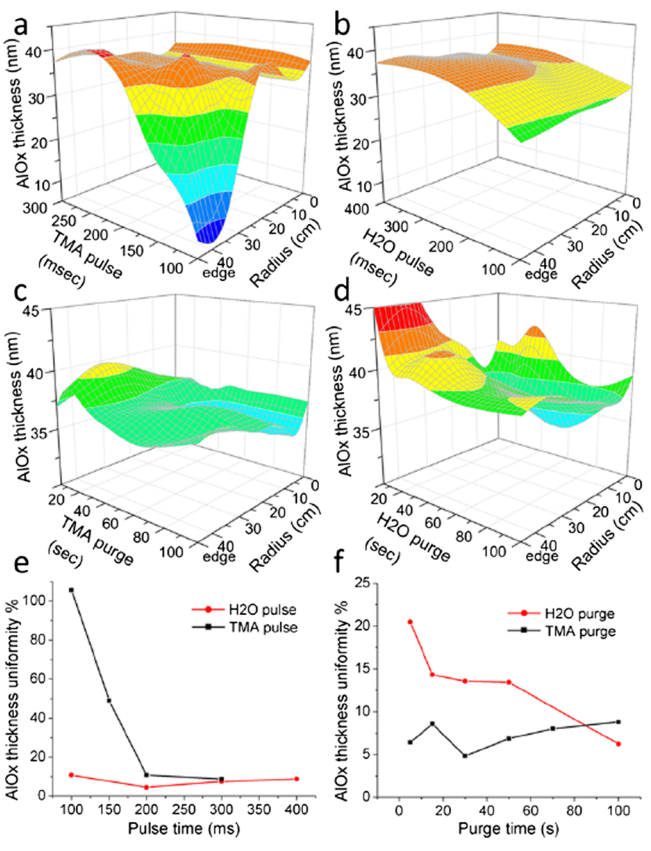

Figure 5. 3D plots of AlO_x thickness vs substrate radius and (a) $t_{TMA\text{-}pulse}$, (b) $t_{H_2O\text{-}pulse}$, (c) $t_{TMA\text{-}purge}$, and (d) $t_{H_2O\text{-}purge}$ indicate that saturated growth mode is attained across the substrate radius with sufficiently long pulse and purge times. The pulse/purge time axis direction varies from (a,b) to (c,d) to best display the 3D curve features. AlO_x thickness uniformity across the chamber radius vs (e) precursor pulse time and (f) precursor purge time shows a simplified indication of saturated growth mode with sufficiently long pulse and purge times.

With respect to the well-understood chemistry of TMA and H_2O, the saturation growth curves in Figure 5 demonstrate contrast in uniformity and growth rate dependency on both pulse and purge times of each precursor. As the TMA pulse time ($t_{TMA\text{-}pulse}$) decreases from the saturated growth rate regime, the AlO_x thickness decreases at the edge of the chamber radius relative to the chamber center, resulting in poor uniformity, shown in Figure 5a,e. However, as the H_2O pulse time ($t_{H_2O\text{-}pulse}$) decreases from the saturated growth rate regime, the thickness decreases equally across the entire radius of the chamber and uniformity is preserved, shown in Figure 5b,e. This contrast in growth rate and uniformity dependence on $t_{TMA\text{-}pulse}$ vs $t_{H_2O\text{-}pulse}$ suggests that TMA vapor is more quickly chemisorbed and efficiently consumed as a complete monolayer as it flows through the chamber, which can be defined as a mass transport-limited reaction, but H_2O vapor is slowly consumed and more likely to pass over all chamber surfaces before being chemisorbed, which can be defined as a surface reaction-limited process. These observations in large-area AlO_x growth rate and uniformity dependence on TMA and H_2O pulse times confirm the common understanding that the TMA half-reaction behaves more ideally in the formation of a self-limited monolayer than the H_2O half-reaction, which is more prone to temperature-sensitive surface reactions resulting in uniformly sparse monolayers or adsorption greater than a monolayer.[56−59]

Growth rate and uniformity also show contrasting dependence on purge times for TMA and H_2O precursors ($t_{TMA\text{-}purge}$ and $t_{H_2O\text{-}purge}$) as shown in Figure 5c,d,f. Varying $t_{TMA\text{-}purge}$ causes relatively less noticeable change in AlO_x thickness and uniformity across the substrate radius in comparison to $t_{H_2O\text{-}purge}$, as shown in Figure 5c. It is expected that the 5 s soak step common to all depositions in this experiment decreases the dependence of AlO_x thickness uniformity on $t_{TMA\text{-}purge}$. TMA is highly volatile and has high vapor pressure, and therefore it is likely that excess TMA quickly desorbs during the 5 s TMA soak step and possibly condenses downstream of the growth chamber in the unheated exhaust lines.[56,57] Variation in $t_{H_2O\text{-}purge}$ yields more noticeable change in AlO_x thickness and uniformity, shown in Figures 5d and 5f. With short $t_{H_2O\text{-}purge}$, the edge of the substrate shows increased thickness when compared to the substrate center. When considering the lower volatility and lower vapor pressure of H_2O vapor, this higher growth rate at the substrate edge may be caused by the "stickiness" and undesired long required pumping time to desorb and remove excess H_2O from a vacuum chamber.[58,59] Because purge gas velocity is expected to decrease from the center to the edge of the chamber as the

DOI: 10.1021/acsami.8b10457
ACS Appl. Mater. Interfaces XXXX, XXX, XXX−XXX

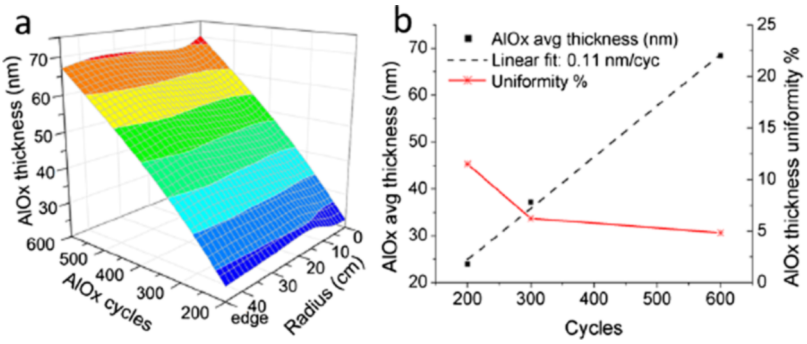

Figure 6. (a) 3D plot of AlO_x thickness vs cycles showing a linear growth rate across the substrate radius. Average growth rate across the substrate radius is shown by (b) AlO_x average thickness vs cycles plotted with a linear fit, and AlO_x thickness uniformity vs cycles shows improved uniformity with increasing cycles.

cross-sectional area of gas flow widens, any boundary layer formation will also experience an increasing gradient from the chamber center to the edge. Desorption and diffusion rates of excess H_2O through the boundary layer are expected to decrease toward the edge of the chamber, and therefore longer pumping times are necessary to ensure uniform removal of excess precursor vapor.

The optimized process parameters listed in Table 1 were selected for further deposition experiments. To ensure that all parameters remained adequately saturated for subsequent experiments, both pulse and purge times were conservatively selected to be slightly longer than what was measured to be the minimum required time necessary for optimal uniformity. Growth rate and uniformity were observed with a varying number of cycles using these parameters to grow AlO_x films for 200, 300, and 600 cycles, plotted in Figure 6a as a 3D color map. Average AlO_x thickness across the substrate radius was plotted with a linear fit in Figure 6b. The slope of the linear fit shows a growth rate of 0.11 nm/cycle, which agrees with reported growth rates demonstrating similar AlO_x films at similar low temperatures using thermal ALD of TMA and H_2O.[28,30,31,36] Figure 6b also shows the AlO_x thickness uniformity across the substrate radius plotted against the number of cycles. As the film thickness increases, uniformity improves, which suggests the presence of local variations in the initial nucleation process across the substrate.

3.2. Thickness Uniformity Mapping. Averaging AlO_x film deposition across the entire measured substrate area, the high-resolution uniformity test yielded an average thickness of 68.5 nm with an average refractive index of 1.60. Although ~90% of the mapped area in Figure 7c has AlO_x thickness within ~1.5% of the average, several localized areas exhibit significantly thicker AlO_x deposition. The center wafer and several wafers around the substrate edge show AlO_x thickness up to 75 nm, represented by dense red spots on the uniformity color map in Figure 7c. Such localized non-uniformity is not a typical characteristic of ALD, even when using growth parameters outside of the calibrated saturated growth mode. When conventional ALD processes exhibit non-uniform growth due to subsaturated precursor pulse/purge times, the resulting film thickness typically decreases following a gradient along the direction of gas flow, as observed in the subsaturated regions of the 3D plots in Figure 5. In contrast to this common pattern of non-uniformity, the localized areas of increased AlO_x thickness in this high-resolution uniformity test of the MSAS are observed on one wafer slightly offset from the gas inlet at the chamber center and on several wafers around the edge near

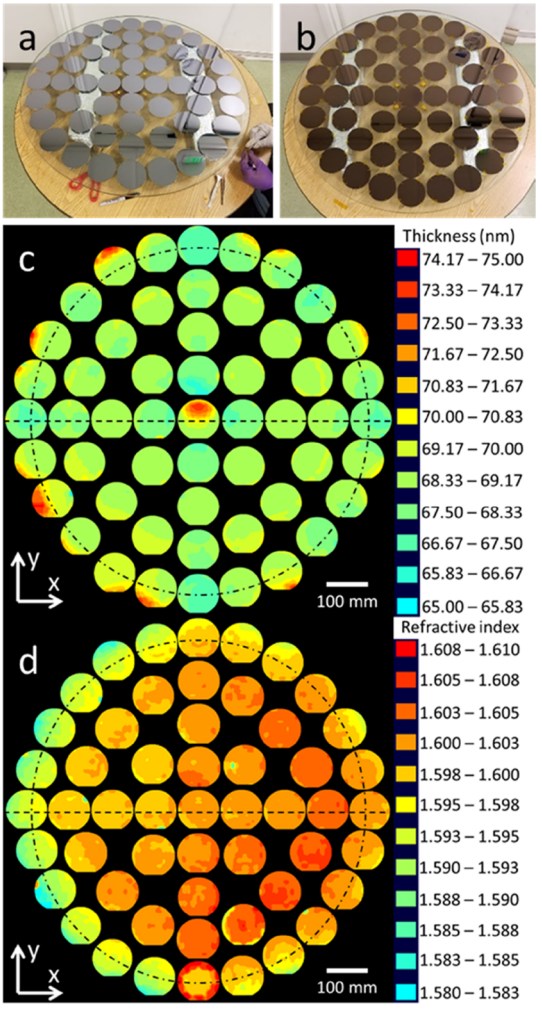

Figure 7. Uniformity test of 600 AlO_x cycles showing 53 100 mm Si wafers arranged on 0.9 m glass substrate (a) being positioned before deposition and (b) uniformly coated after deposition. The four deflection-limiting standoffs are also visible around the center wafer, attached using orange Kapton tape. 2D color uniformity maps of (c) AlO_x thickness and (d) refractive index at λ = 632 nm with dashed lines representing profile plots across substrate x-axis and around substrate circumference 5 cm from edge.

the O-ring seal. Because these two areas of the substrate affected by localized increased thickness are adjacent to O-ring seals, it is possible that the increased AlO_x thickness is caused

DOI: 10.1021/acsami.8b10457
ACS Appl. Mater. Interfaces XXXX, XXX, XXX−XXX

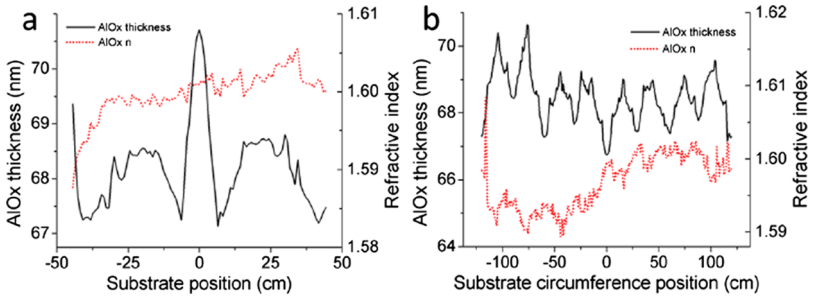

Figure 8. AlO_x thickness and refractive index profiles of (a) substrate *x*-axis and (b) substrate circumference 5 cm from the edge as indicated by dotted lines from Figure 7c,d. Pattern 1 is observed in the linear refractive index of (a), pattern 2 is observed in the linear thickness plotted in (a), and pattern 3 is observed in the circumferential thickness plotted in (b).

by vacuum leaks at these O-ring seals. Because of the high reactivity of metalorganic precursors with ambient oxygen and H_2O, atmospheric leaks into a reaction chamber are significantly detrimental to controlled chemistry processes such as ALD. It is possible that localized regions with increased thickness directly correlate with vacuum leak points. We will investigate and correct this as part of future work.

Besides the localized non-uniform areas of higher film thickness, the uniformity color maps in Figure 7c,d exhibit three characteristic patterns in film thickness and refractive index that are detrimental to overall uniformity. The first pattern (pattern 1) is characterized as a gradient in refractive index, approximately in a linear direction along the *x*-axis, from left to right as viewed in Figure 7d, where there is an observable hemispherical division showing lower refractive index on the left side of the substrate and higher refractive index on the right side. Second (pattern 2), a radially symmetric single-oscillation pattern is observed in the thickness profile of Figure 7c from the substrate center to the edge. Film thickness is higher at the center of the substrate, decreases ∼5 cm from the substrate center, gradually increases in thickness halfway between substrate center and edge (∼20−30 cm), and then decreases in thickness toward the substrate edge (45 cm). Previously discussed AlO_x depositions mapped in Figure 5 also exhibit this single oscillation in thickness along the substrate radius. Third (pattern 3), the thickness profile of the outer circumference of the substrate (5 cm from substrate edge) exhibits a sinusoidal oscillation. This pattern has eight-fold symmetry, which matches the same eight-fold symmetry of the exhaust port placement around the edge of the MSAS chamber baseplate design as shown in Figure 3a.

Profiles of thickness and refractive index profiles along the dashed lines on the uniformity color maps in Figure 7c,d are plotted in Figure 8. The Figure 8a linear profile has a thickness uniformity of ±2.5% and a refractive index uniformity of ±0.6%, and the Figure 8b circumferential thickness profile has a thickness uniformity of ±2.8% and a refractive index uniformity of ±0.6%. Although some anticorrelation between thickness and refractive index is observed in the circumferential profile of Figure 8b, it should be noted that the total optical thickness (the product of refractive index and thickness), which is not shown, demonstrates similar uniformity as the thickness due to the less significant contribution of the small variations in refractive index. Figure 8a effectively displays the gradient in refractive index with linear symmetry (pattern 1) and single oscillating pattern of thickness with radial symmetry (pattern 2), and Figure 8b effectively displays the eight-fold radial symmetry in thickness (pattern 3) observable in the circumferential profile. These three patterns in thickness and refractive index uniformity can be correlated with certain aspects of the MSAS chamber geometry design. Pattern 1 is likely explained by variations in baseplate temperatures, which is plausible given the commonly observed direct relationship between AlO_x refractive index and ALD deposition temperature.[28,30,31,36] The baseplate is heated by eight resistive bar heaters, arranged between the eight exhaust ports with radial symmetry, extending from the chamber center to the edge. Two power supplies independently heat the left and right hemisphere of the baseplate. Although the two power supplies operate with identical control input, it is possible for small variations in the thermocouple calibrations and gain feedback for the two control systems to produce uneven temperatures across the two controlled temperature zones of the baseplate. This baseplate temperature gradient can be corrected by recalibrating thermocouples of both temperature zones confirmed with external temperature measurements.

Pattern 2 can also be correlated with geometrical features of the MSAS baseplate. Increased thickness across the entire 100 mm wafer at the substrate center may correlate with the obviously higher exposure to process gas entering the chamber. Thickness uniformly decreases ∼5 cm from the center, increases again to reach average film thickness (∼68.5 nm) in the center toroidal area ∼13−30 cm from the substrate center, and then falls below average at the 45 cm edge. This thickness pattern correlates with features of the chamber baseplate geometry. At 30 cm from the chamber center, the flow diverting sheet that covers the eight exhaust ports is mounted to a recessed edge in the chamber baseplate. Although the inner portion of the chamber baseplate and the flow diverting sheet are designed to be nominally equal in height and provide a flat smooth path of gas flow, it is possible that the transition between the inner baseplate portion and flow diverting sheet directly influence the oscillation pattern in thickness along the radius seen in Figures 7c and 8a. The gradient in the actual chamber height due to the controlled deflection of the glass substrate from 2 mm at the chamber center to 5 mm at the edge contributes to the increasing gas flow cross-sectional area from the chamber center to the edge, which is expected to dominate any small unintentional changes in chamber geometry caused by the seam transition between the inner baseplate surface and the flow diverting sheet. While there is a small seam in the baseplate profile that may possibly affect the gas flow pattern, the thermal coupling between the flow diverting sheet and the baseplate may also affect the local surface temperature of the substrate. A refractive index step is also observable just beyond the 30 cm seam (∼35 cm) in the

DOI: 10.1021/acsami.8b10457
ACS Appl. Mater. Interfaces XXXX, XXX, XXX−XXX

2D color map in Figure 7d and the linear profile in Figure 8a. The combination of changing gas velocity and temperature from the center to the outside of the baseplate may affect the AlO_x growth rate to produce the radially symmetric single oscillation in thickness of pattern 2.

Pattern 3, shown by the circumferential thickness profile in Figure 8b, follows the same eight-fold symmetrical pattern of the exhaust ports around the baseplate circumference, as seen in Figure 3a from a top-down view of the chamber baseplate. Increased growth rate above the eight chamber exhaust ports, like pattern 2, may also be attributed to a combination of possible gradients in temperature and process gas velocity. While the local chamber or substrate temperature has not been spatially mapped, the unheated exhaust ports are expected to act as heat sinks which may decrease the local chamber temperature around the exhaust ports and the corresponding substrate areas above the ports. Simulated gas velocity in the MSAS chamber at 0.1 Torr, shown in the 3D color map in Figure 2d, exhibits a gas velocity pattern with eight-fold symmetry similar to the thickness uniformity pattern observable in Figures 7c and 8b, with higher velocity above the eight exhaust ports and lower velocity in the chamber edge regions between exhaust ports. The possibility of gas flow-dependent non-uniform precursor exposure in the MSAS is unlikely in this work, because the 5 s soak step used after every precursor pulse disrupts steady-state gas flow patterns and instead allows more time for uniform precursor diffusion throughout the entire chamber. While the simulated gas velocity patterns showing moderate eight-fold symmetry in Figure 2 cannot be applied to precursor vapor distribution during the soak steps with no steady-state gas flow, they may be applicable to purge gas velocity patterns, which may affect the localized growth rate dependent on the amount of excess H_2O removed when purging. As desorption and diffusion rates decrease from the chamber center to edge due to decreasing gas velocity and increasing boundary layer thickness, these rates will also further decrease with any localized areas of slower purge gas velocity around the outer edge of the chamber, which is expected to occur in the periodic chamber edge areas between exhaust ports.

We suggest that the eight-fold pattern in film thickness uniformity of pattern 3 and the single radial oscillation of pattern 2 are caused by a combination of spatial gradients in temperature and gas flow during H_2O purging across the substrate. Because the desorption rate of H_2O is dependent on both temperature and purge gas flow, this initial uniformity mapping experiment will need to be supplemented with further deposition and characterization data to quantitatively decouple effects of non-uniformity in gas flow and temperature on growth rate and uniformity. We are modifying the MSAS to adequately heat and monitor temperature of localized chamber areas, particularly the exhaust ports, and installing additional flow diverters. Additional CFD simulations suggest that uniformity of gas velocity and fluid density can be further optimized by implementing new flow diverting hardware designs. A simple simulation of a redesigned chamber exhaust configuration with 16 ports distributed around the baseplate perimeter at even intervals shows fluid density uniformity of ±1%; this is a simple and significant improvement from the simulated fluid density uniformity of ±3%, resulting from simulations using the current 8-port exhaust configuration demonstrated in this study.[52]

3.3. Comparing Deposition Parameters of 100 mm to 0.9 m Substrate.

Table 2 lists the optimized process parameters, the reaction chamber parameters, and growth results for the MSAS and the conventional ("small") system. The right-hand column lists the calculated ratio for each parameter. These results show that to a remarkable degree, the parameter ratios scale as expected. Precursor pulse times 5−6 times longer are required for saturated AlO_x deposition using the MSAS compared to conventional single wafer chamber deposition, and purge times are relatively similar. Saturated ALD growth in the MSAS with 6× more total chamber volume is expected to require more precursor and surface area than the small ALD chamber. However, the closely matching ratios of precursor pulse time and chamber volume and surface area between the deposition processes of the MSAS and small reactor suggests that the calculation and scaling mechanism for ALD reactions with larger chambers may be relatively simple to predict. Because the two reactors used comparable reaction temperature, gas flow, precursor source temperature, precursor delivery valves, and pumping hardware, the total increase in precursor caused by increasing pulse time is expected to be similar in both ALD systems. A 6× longer precursor pulse exposure of TMA in the MSAS is expected to deliver ∼6× the TMA into 6× the volume and therefore produce a comparable TMA partial pressure to that of the TMA partial pressure in the small ALD chamber. Precursor purge times, which have been shown to be highly dependent on reactor temperature and pressure,[28,29,57] were expected to be comparable between the two reactors. However, because this study focused on achieving the excellent uniformity typically expected of the ALD process, purge times for both precursors in both reactors were set conservatively longer than the minimum required purge times to ensure that depositions were optimized for best uniformity. Therefore, we do not consider the demonstrated optimized purge times in Table 2 to represent as accurate of a comparison between the two reactors as compared to the pulse times used in both reactors, which were more carefully tuned to best study the expected scalability between the two reactors. However, it will be critical to optimize purge times in an ALD process practically applied in a routine deposition system, which would be required for coating telescope mirrors in an

Table 2. Process Parameters, System Parameters, and Growth Results Comparing the MSAS and a Conventional Single Wafer-Scale ALD System (Small) for 300 Cycles of AlO_x Deposited at 60 °C, with Scaling Ratios Listed for the Process and System Parameters

AlO_x growth process parameter	MSAS	small	ratio
$t_{TMA\text{-}pulse}$ (ms)	300	50	6
$t_{H_2O\text{-}pulse}$ (ms)	400	80	5
$t_{TMA\text{-}purge}$ (s)	30	30	1
$t_{H_2O\text{-}purge}$ (s)	50	30	1.7
System Parameter			
total chamber volume (cm^3)	14 000	2330	6
total chamber surface area (cm^2)	30 400	4900	6.2
pumping speed (m^3)/h at 75 mTorr	85	82	1
base pressure (rated; mTorr)	7.5	8	0.9
Results			
demonstrated substrate area (cm^2)	6362	79	81
average growth rate (nm/cyc)	0.11	0.10	
lateral thickness uniformity (%)	5	1	

DOI: 10.1021/acsami.8b10457
ACS Appl. Mater. Interfaces XXXX, XXX, XXX−XXX

observatory. We also expect that an eventual ALD-based protected Ag mirror coating process will not rely on H_2O vapor, but instead use a more volatile oxidizing reactant with higher vapor pressure that enables high-quality thin-film deposition at low temperatures with shorter purge times, such as ozone or oxygen plasma for oxides, or ammonia or nitrogen plasma for nitrides.

We propose that, to first order, the thermal ALD chemistry of TMA and H_2O can be simply scaled from a well-calibrated small reactor to larger chamber sizes by increasing the total precursor exposure amount by the same factor of increased chamber volume. It should be noted that increased precursor exposure can be accomplished several ways, including: extending the precursor valve pulse time (as in this study), heating precursor containers to increase partial vapor pressure at the source, or by actively pushing precursor vapor with carrier gas using a "bubbler" CVD delivery configuration for longer pulse times. This third method of increasing precursor delivery is common if precursors with low vapor pressure are required to deposit films at low substrate temperatures,[28,36] and we suggest that bubbler precursor delivery will likely be necessary to achieve uniform ALD film growth in chambers ~10× larger than the MSAS chamber demonstrated in this study.

We predict that this study in scalability can and will be used to further increase the feasible substrate size in such a large-area chamber design. Using this substrate/chamber wall technique, similar high-quality ALD thin films may be practically applied to optical substrates as AR coatings on large-aperture lenses or as protective barriers on the 1.4 m segments of the TMT primary mirror. With an established scalable deposition process of low-temperature AlO_x, future work will utilize the scaling process parameters identified in Table 2 to study scalability of different thin-film chemistry processes in the MSAS. While AlO_x is generally a proficient corrosion barrier for many applications, extensive studies have shown that it is not an optimized stand-alone coating material to protect against environmental corrosion because of its eventual dissolution from atmospheric moisture.[60−65] Therefore, future work will explore low-temperature deposition processes with the MSAS of thin-film materials that have shown promising corrosion barrier properties on Ag in previous work when deposited by PVD techniques, such as TiO_2 and Si_3N_4.[5−9] The optimized process conditions and lessons in this work will be used to further optimize MSAS process performance for metal oxide thin films, specifically with the use of alternative oxidizing reactants that can be purged quicker than H_2O, such as ozone, oxygen plasma, and wet Ar plasma. Detecting and eliminating vacuum leaks, minimizing gas flow-dependent growth patterns with improved flow diverting hardware, and precisely calibrating and controlling chamber and substrate temperatures are unique challenges of this new large-area ALD technique that will be addressed in future work exploring protected Ag mirror barrier coatings.

4. CONCLUSIONS

Low-temperature AlO_x deposition has been demonstrated across a 0.9 m substrate in the large-area MSAS chamber with a 1 m diameter scale of deposition. The well-understood ALD reaction of TMA and H_2O has been shown to scale up to the larger 0.9 m substrate by calibrating and optimizing saturated ALD growth mode in a fashion similar to conventional wafer-scale ALD chamber process optimization. Both film thickness uniformity across the substrate and growth rate are shown to be significantly important in establishing saturated ALD growth mode in the MSAS. High-resolution uniformity mapping of film thickness and refractive index was used to analyze the effect of MSAS chamber design and deposition parameters on resulting AlO_x film uniformity patterns. Linear profiles show thickness uniformity within 2.5% of average film thickness. Elimination of vacuum leaks, ex situ chamber temperature calibration, and increased flow diverting baffling hardware are discussed as possible methods of further improving uniformity. The low-temperature AlO_x ALD process was compared between the MSAS reactor and a conventional 100 mm wafer-scale reactor, and a direct relationship is suggested between increasing chamber size and precursor dose necessary to scale up a saturated ALD growth process. The chamber design and resulting deposition uniformity shown here support the possible application of ALD thin-film corrosion barriers to large-area substrates.

AUTHOR INFORMATION

Corresponding Author

*E-mail: dfryauf@ucsc.edu.

ORCID

David M. Fryauf: 0000-0001-7019-2827

Notes

The authors declare no competing financial interest.

ACKNOWLEDGMENTS

We would like to thank Gary Provost, Tom Salajaj, and the rest of the staff and engineers at Structured Materials Industries, Inc. for their extensive work and collaboration in the design, construction, and installation of the MSAS. We thank Director Claire Max for continued support of coatings research at UCO. Brian Dupraw, Chris Ratliff, Matt Radovan, and Alex Tripsas provided much-appreciated additional help at UCO. Faiza Anjum, Brian Giraldo, Ravipa Losakul, Mingran Liu, and Emmanuel Kayede from the NECTAR lab have directly enabled this research by helping load and unload the 25 kg glass substrate numerous times. We owe many thanks and original credit to Joe Miller, who inspired the development of ALD coatings at the UCO Advanced Coatings Lab. We gratefully acknowledge our support by the National Science Foundation from the following Award numbers: 1407353, "ALD Barrier Layers on Large Silver-coated Mirrors" (with thanks to the program officer, Dr. Peter Kurczynski); 1562634, "Study of Surface Templates Nanomanufactured for Growing Single-Crystal Semiconductor Films," with support from Dr. Khershed Cooper.

REFERENCES

(1) Jacobson, M. R.; Kneale, R.; Raybould, K.; Gillett, F. C.; Laird, R.; Shimshock, R. P.; Booth, D. C. Development of Silver Coating Options for the Gemini 8-m Telescopes Project. *Proc. SPIE* **1998**, *3352*, 477−502.

(2) Boccas, M.; Vucina, T.; Araya, C.; Vera, E.; Ahhee, C. Coating the 8-m Gemini Telescopes with Protected Silver. *Proc. SPIE* **2004**, *5494*, 239.

(3) Vucina, T.; Boccas, M.; Araya, C.; Ah Hee, C.; Cavedoni, C. Gemini Primary Mirror in-situ Wash. *Proc. SPIE* **2008**, *7012*, 70122Q.

(4) Schneider, T.; Vucina, T.; Ah Hee, C.; Araya, C.; Moreno, C. The Gemini Observatory Protected Silver Coating: Ten Years in Operation. *Proc. SPIE* **2016**, *9906*, 990632.

DOI: 10.1021/acsami.8b10457
ACS Appl. Mater. Interfaces XXXX, XXX, XXX−XXX

(5) Phillips, A. C.; Miller, J.; Brown, W. E.; Hilyard, D.; Dupraw, B.; Wallace, V.; Cowley, D. Progress Toward High-Performance Reflective and Anti-Reflection Coatings for Astronomical Optics. *Proc. SPIE* **2008**, *7018*, 70185A.
(6) Phillips, A. C.; Brown, W. E.; Dupraw, B.; Hilyard, D. F.; Cowley, D. J. Progress Toward High-Performance Astronomical Coatings. *Proc. SPIE* **2010**, *7739*, 77393Y.
(7) Phillips, A. C.; Miller, J. S.; Bolte, M.; DuPraw, B.; Radovan, M. V.; Cowley, D. J. Progress in UCO's Search for Silver-Based Telescope Mirror Coatings. *Proc. SPIE* **2012**, *8450*, 84502G.
(8) Phillips, A. C.; Fryauf, D. M.; Kobayashi, N. P.; Bolte, M.; DuPraw, B.; Ratliff, C.; Cowley, D.; Pfister, T. Progress and New Techniques for Protected-Silver Coatings. *Proc. SPIE* **2014**, *9151*, 91511B.
(9) Phillips, A. C.; Fryauf, D. M.; Kobayashi, N. P.; DuPraw, B.; Cheleden, S.; Ratliff, C.; Bolte, M. J.; Cowley, D. Update on UCO's Advanced Coating Lab Development of Silver-Based Mirror Coatings. *Proc. SPIE* **2016**, *9912*, 99122G.
(10) TMT Science-Based Requirements Document. https://www.tmt.org/download/Document/11/original (accessed May 11, 2018).
(11) McPeak, K. M.; Jayanti, S. V.; Kress, S. J. P.; Meyer, S.; Iotti, S.; Rossinelli, A.; Norris, D. J. Plasmonic Films Can Easily be Better: Rules and Recipes. *ACS Photonics* **2015**, *2*, 326−333.
(12) Hutcheson, E. T.; Hass, G.; Coulter, J. K. A direct comparison of the visible and ultraviolet reflectance of aluminum films evaporated in conventional and ultra-high vacuum systems. *Opt. Commun.* **1971**, *3*, 213−216.
(13) Bourque, A. J.; Gurian, J. H. High Reflectivity Large Scale Telescope Mirror Coatings via Long Throw Sputtering. *Proc. SPIE* **2014**, *9151*, 91515J.
(14) Limam, E.; Maurice, V.; Seyeux, A.; Zanna, S.; Klein, L. H.; Chauveau, G.; Grèzes-Besset, C.; De Larclause, I. S.; Marcus, P. Local Degradation Mechanisms by Tarnishing of Protected Silver Mirror Layers Studied by Combined Surface Analysis. *J. Phys. Chem. B* **2017**, *122*, 578−586.
(15) Hu, C.; Liu, J.; Wang, J.; Gu, Z.; Li, C.; Li, Q.; Li, Y.; Zhang, S.; Bi, C.; Fan, X.; Zheng, W. New Design for Highly Durable Infrared-Reflective Coatings. *Light: Sci. Appl.* **2018**, *7*, 17175.
(16) Bartzsch, H.; Frach, P.; Weber, J.; Liebig, J. S. Precision Optical and Antireflection Multilayer and Gradient Coatings Containing Reactively Sputtered Oxides, Nitrides and Fluorides. *Proc. SPIE* **2005**, *5963*, 59631B.
(17) Raut, H. K.; Ganesh, V. A.; Nair, A. S.; Ramakrishna, S. Anti-Reflective Coatings: A Critical, in-Depth Review. *Energy Environ. Sci.* **2011**, *4*, 3779−3804.
(18) Mazur, M.; Wojcieszak, D.; Domaradzki, J.; Kaczmarek, D.; Song, S.; Placido, F. TiO2/SiO2 Multilayer as an Antireflective and Protective Coating Deposited by Microwave Assisted Magnetron Sputtering. *Opto-Electron. Rev.* **2013**, *21*, 233−238.
(19) León, J. J. D.; Garrett, M. P.; Zhang, J.; Kobayashi, N. P. Aluminum Titanium Oxide Alloys: Deposition of Amorphous, Transparent, Corrosion-Resistant Films by Pulsed DC Reactive Magnetron Sputtering with RF Substrate Bias. *Mater. Sci. Semicond. Process.* **2015**, *36*, 96−102.
(20) Xu, X.; He, W.; Wang, C.; Wei, M.; Li, B. SiNx thickness dependence of spectral properties and durability of protected-silver mirrors. *Surf. Coat. Technol.* **2017**, *324*, 175−181.
(21) Sheikh, D. A. Improved Silver Mirror Coating for Ground and Space-Based Astronomy. *Proc. SPIE* **2016**, *9912*, 991239.
(22) Dennler, G.; Houdayer, A.; Raynaud, P.; Séguy, I.; Ségui, Y.; Wertheimer, M. R. Growth Modes of SiOx Films Deposited by Evaporation and Plasma-Enhanced Chemical Vapor Deposition on Polymeric Substrates. *Plasmas Polym.* **2003**, *8*, 43−59.
(23) Uchida, H.; Inoue, S.; Koterazawa, K. Electrochemical evaluation of pinhole defects in TiN films prepared by r.f. reactive sputtering. *J. Mater. Sci. Eng. A* **1997**, *234−236*, 649−652.
(24) Chatham, H. Oxygen Diffusion Barrier Properties of Transparent Oxide Coatings on Polymeric Substrates. *Surf. Coat. Technol.* **1996**, *78*, 1−9.
(25) Panjan, P.; Čekada, M.; Panjan, M.; Kek-Merl, D.; Zupanič, F.; Čurković, L.; Paskvale, S. Surface Density of Growth Defects in Different PVD Hard Coatings Prepared by Sputtering. *Vacuum* **2012**, *86*, 794−798.
(26) Díaz León, J. J.; Garrett, M. P.; Zhang, J.; Kobayashi, N. P. Aluminum Titanium Oxide Alloys: Deposition of Amorphous, Transparent, Corrosion-Resistant Films by Pulsed DC Reactive Magnetron Sputtering with RF Substrate Bias. *Mater. Sci. Semicond. Process.* **2015**, *36*, 96−102.
(27) Fryauf, D. M.; Leon, J. J. D.; Phillips, A. C.; Kobayashi, N. P. Effect of Intermediate Layers on Atomic Layer Deposition-Aluminum Oxide Protected Silver Mirrors. *J. Astronomical Telesc. Instrum. Syst.* **2017**, *3*, 034001.
(28) George, S. M. Atomic Layer Deposition: an Overview. *Chem. Rev.* **2009**, *110*, 111−131.
(29) Puurunen, R. L. Surface Chemistry of Atomic Layer Deposition: A Case Study for the Trimethylaluminum/Water Process. *J. Appl. Phys.* **2005**, *97*, 121301.
(30) Elam, J. W.; Groner, M. D.; George, S. M. Viscous Flow Reactor with Quartz Crystal Microbalance for Thin Film Growth by Atomic Layer Deposition. *Rev. Sci. Instrum.* **2002**, *73*, 2981−2987.
(31) Groner, M. D.; Fabreguette, F. H.; Elam, J. W.; George, S. M. Low-Temperature Al2O3Atomic Layer Deposition. *Chem. Mater.* **2004**, *16*, 639−645.
(32) Schwinde, S.; Schürmann, M.; Jobst, P. J.; Kaiser, N.; Tünnermann, A. Description of Particle Induced Damage on Protected Silver Coatings. *Appl. Opt.* **2015**, *54*, 4966−4971.
(33) Fryauf, D. M.; Phillips, A. C.; Kobayashi, N. P. Corrosion Barriers for Silver-Based Telescope Mirrors: Comparative Study of Plasma-Enhanced Atomic Layer Deposition and Reactive Evaporation of Aluminum Oxide. *J. Astronomical Telesc. Instrum. Syst.* **2015**, *1*, 044002.
(34) Folgner, K. A.; Chu, C.-T.; Lingley, Z. R.; Kim, H. I.; Yang, J.-M.; Barrie, J. D. Environmental Durability of Protected Silver Mirrors Prepared by Plasma Beam Sputtering. *Appl. Opt.* **2017**, *56*, C75−C86.
(35) Fryauf, D. M.; Diaz Leon, J. J.; Phillips, A. C.; Kobayashi, N. P. Silver Film Surface Modification by Ion Bombardment Decreases Surface Plasmon Resonance Absorption. *ACS Appl. Mater. Interfaces* **2017**, *9*, 15841−15847.
(36) Miikkulainen, V.; Leskelä, M.; Ritala, M.; Puurunen, R. L. Crystallinity of Inorganic Films Grown by Atomic Layer Deposition: Overview and General Trends. *J. Appl. Phys.* **2013**, *113*, 021301.
(37) Profijt, H. B.; Potts, S. E.; van de Sanden, M. C. M.; Kessels, W. M. M. Plasma-Assisted Atomic Layer Deposition: Basics, Opportunities, and Challenges. *J. Vac. Sci. Technol., A* **2011**, *29*, 050801.
(38) Schwille, M. C.; Schössler, T.; Schön, F.; Oettel, M.; Bartha, J. W.; Höchst, A.; Oettel, M.; Bartha, J. W. Temperature dependence of the sticking coefficients of bis-diethyl aminosilane and trimethylaluminum in atomic layer deposition. *J. Vac. Sci. Technol., A* **2017**, *35*, 01B119.
(39) Pan, D.; Ma, L.; Xie, Y.; Wang, F.; Jen, T.-C.; Yuan, C. Experimental and Numerical Investigations into the Transient Multi-Wafer Batch Atomic Layer Deposition Process with Vertical and Horizontal Wafer Arrangements. *Int. J. Heat Mass Transfer* **2015**, *91*, 416−427.
(40) Elam, J. W.; Routkevitch, D.; Mardilovich, P. P.; George, S. M. Conformal Coating on Ultrahigh-Aspect-Ratio Nanopores of Anodic Alumina by Atomic Layer Deposition. *Chem. Mater.* **2003**, *15*, 3507−3517.
(41) Wang, G.; Xu, Q.; Yang, T.; Xiang, J.; Xu, J.; Gao, J.; Li, C. Application of Atomic Layer Deposition Tungsten (ALD W) as Gate Filling Metal for 22 nm and Beyond Nodes CMOS Technology. *ECS J. Solid State Sci. Technol.* **2014**, *3*, P82−P85.
(42) Knoops, H. C. M.; Langereis, E.; van de Sanden, M. C. M.; Kessels, W. M. M. Conformality of Plasma-Assisted ALD: Physical Processes and Modeling. *J. Electrochem. Soc.* **2010**, *157*, G241−G249.
(43) Bosund, M.; Salmi, E. M.; Peltonen, R. *Atomic Layer Deposition into Ultra-High Aspect Ratio Structures with a Stop-Flow ALD Reactor*, 2016 www.beneq.com.

DOI: 10.1021/acsami.8b10457
ACS Appl. Mater. Interfaces XXXX, XXX, XXX−XXX

(44) Fryauf, D. M.; Norris, K. J.; Zhang, J.; Kobayashi, N. P.; Wang, S.-Y. Titanium Oxide Vertical Resistive Random-Access Memory Device. *Micro Nano Lett.* **2015**, *10*, 321−323.
(45) Fryauf, D. M.; Zhang, J.; Norris, K. J.; Diaz Leon, J. J.; Oye, M. M.; Wei, M.; Kobayashi, N. P. Photoluminescence Blue Shift of Indium Phosphide Nanowire Networks with Aluminum Oxide Coating. *Phys. Status Solidi RRL* **2014**, *8*, 663−667.
(46) Sneh, O.; Clark-Phelps, R. B.; Londergan, A. R.; Winkler, J.; Seidel, T. E. Thin Film Atomic Layer Deposition Equipment for Semiconductor Processing. *Thin Solid Films* **2002**, *402*, 248−261.
(47) Poodt, P.; Cameron, D. C.; Dickey, E.; George, S. M.; Kuznetsov, V.; Parsons, G. N.; Roozeboom, F.; Sundaram, G.; Vermeer, A. Spatial Atomic Layer Deposition: A Route Towards Further Industrialization of Atomic Layer Deposition. *J. Vac. Sci. Technol., A* **2012**, *30*, 010802.
(48) Skarp, J. I. High Throughput ALD Production Systems for Cadmium Free CIGS and Enhanced Efficiency c-Si Solar Cells. *ECS Trans.* **2010**, *33*, 447−452.
(49) Putkonen, M. I. ALD Applications Beyond Outside IC Technology-Existing and Emerging Possibilities. *ECS Trans.* **2009**, *25*, 143−155.
(50) Huang, H.; Lv, J.; Bao, Y.; Xuan, R.; Sun, S.; Sneck, S.; Li, S. Data of ALD Al 2 O 3 rear surface passivation, Al 2 O 3 PERC cell performance, and cell efficiency loss mechanisms of Al 2 O 3 PERC cell. *Data Brief* **2017**, *11*, 19−26.
(51) Kersten, F.; Förster, I.; Peters, S. Evaluation of Spatial ALD of Al2O3 for Rear Surface Passivation of MC-Si PERC Solar Cells. *Proceedings of 32nd European Photovoltaic Solar Energy Conference and Exhibition*, 2016; Vol. *32*, pp 943−945.
(52) Fryauf, D. M.; Phillips, A. C.; Bolte, M. J.; Feldman, A.; Tompa, G. S.; Kobayashi, N. P. Low-Temperature Atomic Layer Deposition of Aluminum Oxide Scaled up to a 36" Chamber for Observatory Optics. *Proc. SPIE* **2018**, *10706*, 107065D.
(53) Rosental, A.; Adamson, P.; Gerst, A.; Koppel, H.; Tarre, A. Atomic Layer Deposition in Traveling-Wave Reactor: In Situ Diagnostics by Optical Reflection. *Appl. Surf. Sci.* **1997**, *112*, 82−86.
(54) Mousa, M. B. M.; Oldham, C. J.; Parsons, G. N. Precise Nanoscale Surface Modification and Coating of Macroscale Objects: Open-Environment in loco Atomic Layer Deposition on an Automobile. *ACS Appl. Mater. Interfaces* **2015**, *7*, 19523−19529.
(55) Lubitz, M.; Medina, P. A., IV; Antic, A.; Rosin, J. T.; Fahlman, B. D. Cost-Effective Systems for Atomic Layer Deposition. *J. Chem. Educ.* **2014**, *91*, 1022−1027.
(56) Larrabee, T. J.; Mallouk, T. E.; Allara, D. L. An Atomic Layer Deposition Reactor with Dose Quantification for Precursor Adsorption and Reactivity Studies. *Rev. Sci. Instrum.* **2013**, *84*, 014102.
(57) Salami, H.; Poissant, A.; Adomaitis, R. A. Anomalously High Alumina Atomic Layer Deposition Growth per Cycle During Trimethylaluminum Under-Dosing Conditions. *J. Vac. Sci. Technol., A* **2017**, *35*, 01B101.
(58) Matero, R.; Rahtu, A.; Ritala, M.; Leskelä, M.; Sajavaara, T. Effect of Water Dose on the Atomic Layer Deposition Rate of Oxide Thin Films. *Thin Solid Films* **2000**, *368*, 1−7.
(59) Poodt, P.; Mameli, A.; Schulpen, J.; Kessels, W. M. M.; Roozeboom, F. Effect of Reactor Pressure on the Conformal Coating Inside Porous Substrates by Atomic Layer Deposition. *J. Vac. Sci. Technol., A* **2017**, *35*, 021502.
(60) Maindron, T.; Aventurier, B.; Ghazouani, A.; Jullien, T.; Rochat, N.; Simon, J.; Viasnoff, E. Investigation of Al2O3 Barrier Film Properties Made by Atomic Layer Deposition onto Fluorescent Tris-(8-hydroxyquinoline) Aluminium Molecular Films. *Thin Solid Films* **2013**, *548*, 517−525.
(61) Kim, L. H.; Kim, K.; Park, S.; Jeong, Y. J.; Kim, H.; Chung, D. S.; Kim, S. H.; Park, C. E. Al2O3/TiO2 Nanolaminate Thin Film Encapsulation for Organic Thin Film Transistors via Plasma-Enhanced Atomic Layer Deposition. *ACS Appl. Mater. Interfaces* **2014**, *6*, 6731−6738.
(62) Nehm, F.; Klumbies, H.; Richter, C.; Singh, A.; Schroeder, U.; Mikolajick, T.; Mönch, T. Breakdown and Protection of ALD Moisture Barrier Thin Films. *ACS Appl. Mater. Interfaces* **2015**, *7*, 22121−22127.
(63) Yoon, K. H.; Kim, H. S.; Han, K. S.; Kim, S. H.; Lee, Y.-E. K.; Shrestha, N. K.; Song, S. Y.; Sung, M. M. Extremely High Barrier Performance of Organic−Inorganic Nanolaminated Thin Films for Organic Light-Emitting Diodes. *ACS Appl. Mater. Interfaces* **2017**, *9*, 5399−5408.
(64) Bulusu, A.; Kim, H.; Samet, D.; Graham, S., Jr. Improving the Stability of Atomic Layer Deposited Alumina Films in Aqueous Environments with Metal Oxide Capping Layers. *J. Phys. D: Appl. Phys.* **2013**, *46*, 084014.
(65) Park, S.-K.; Oh, J.; Hwang, C.-S.; Lee, J.-I.; Yang, Y. S.; Chu, H. Y. Ultrathin Film Encapsulation of an OLED by ALD. *Electrochem. Solid-State Lett.* **2005**, *8*, H21−H23.

DOI: 10.1021/acsami.8b10457
ACS Appl. Mater. Interfaces XXXX, XXX, XXX−XXX